

Cite this: *Soft Matter*, 2012, **8**, 6015

www.rsc.org/softmatter

PAPER

## Relationship between microstructure and mechanical properties in spider silk fibers: identification of two regimes in the microstructural changes

Gustavo R. Plaza,<sup>\*ad</sup> José Pérez-Rigueiro,<sup>ad</sup> Christian Riekkel,<sup>b</sup> G. Belén Perea,<sup>ad</sup> Fernando Agulló-Rueda,<sup>c</sup> Manfred Burghammer,<sup>b</sup> Gustavo V. Guinea<sup>ad</sup> and Manuel Elices<sup>ad</sup>

Received 25th February 2012, Accepted 2nd April 2012

DOI: 10.1039/c2sm25446h

The relationship between microstructure and mechanical properties has been investigated in *Argiope trifasciata* dragline silk fibers (major ampullate silk, MAS) by X-ray diffraction, Raman spectroscopy and tensile testing. We have analyzed three fractions of the material, *i.e.* amorphous, highly oriented nanocrystals and weakly oriented material, for different values of the macroscopic alignment parameter  $\alpha$ , calculated as the relative difference between the length of the fiber and its length when supercontracted. Two distinct regimes have been identified: for low values of the alignment parameter  $\alpha$ , microstructural changes are dominated by the reorientation of the nanocrystals; however, at high values ( $\alpha > 0.5$ ) of the alignment parameter, an increase in the fraction of the crystalline phase is revealed. The two regimes are also reflected in the mechanical behaviour, which can be explained by microstructural changes. This finding of the two distinct regimes in the microstructural evolution, which separates the reorientation and the increase in the crystalline phase, will be valuable to develop and validate molecular models of natural and artificial silk fibers, as well as to deepen our present knowledge of the origin of the outstanding properties of MAS fibers. In addition, we have analyzed the characteristics of the crystal lattice, and discussed the relationship between the percentage of short side-chain residues and the unit cell dimensions in different silks.

### I. Introduction

Spider silk fibers are among the most attractive of biological materials. Their outstanding mechanical properties triggered their study within the frame of materials science to unveil the relationship between composition, processing and properties of silk fibers, and nowadays we seek to design artificial silk fibers with the desired properties by means of biotechnology. Despite our, to date, limited knowledge, silk-based materials have been present in a growing set of high-technology applications during the last decade.<sup>1</sup> However, the development of bioinspired fibers has shown that the understanding acquired by the study of natural silk fibers, particularly spider dragline silk fibers, is a critical step in the rational design and production of future high performance fibers.<sup>2</sup>

Silks are semicrystalline polymers of proteins. The most studied spider silk is the dragline silk spun by the major ampullate gland (MAS fibers) in orbicularian spiders. This silk contains two proteins, MaSp1 and MaSp2, whose sequences are partially or completely known for a small number of species,<sup>3</sup> including *Argiope trifasciata* used in this work. A common feature of these proteins is the high content of glycine and alanine. Poly-alanine segments are the main components of anti-parallel  $\beta$ -sheet nanocrystals with an orthorhombic unit cell.<sup>4,5</sup> These nanocrystals, oriented preferentially along the fiber axis, have dimensions of a few nanometres and could constitute over 10% of the silk volume.<sup>6–8</sup> Most of the volume is occupied by amorphous domains formed presumably by the glycine-rich blocks. This fraction includes  $3_{10}$  helices,  $\beta$ -turn or  $\beta$ -spirals, as shown by solid state NMR<sup>9–11</sup> and Raman spectroscopy.<sup>12</sup> Furthermore, the existence of a third phase has been proposed, consisting of weakly oriented crystalline regions of unaggregated  $\beta$ -sheets<sup>6</sup> or ‘oriented amorphous’ material.<sup>7,8</sup> In this article we identify the third phase detected by X-ray diffraction as a weakly oriented material.

The study of the changes induced in the microstructure of MAS fibers by deformation is key to understand the relationship between microstructure and mechanical behavior, and to explain the outstanding properties of silk fibers. In this context, it is reasonable to assume that changes related to the most extreme modification of the properties of silk, *i.e.* supercontraction,

<sup>a</sup>Departamento de Ciencia de Materiales, Universidad Politécnica de Madrid, ETSI de Caminos, Canales y Puertos, 28040 Madrid, Spain. E-mail: gplaza@mater.upm.es

<sup>b</sup>European Synchrotron Radiation Facility, B.P. 220, F-38043 Grenoble Cedex, France

<sup>c</sup>Instituto de Ciencia de Materiales de Madrid (ICMM-CSIC), Cantoblanco, 28049 Madrid, Spain

<sup>d</sup>Center for Biomedical Technology, Universidad Politécnica de Madrid, 28040 Madrid, Spain

should cast light on the microstructural changes associated with the deformation of the fibers. Supercontraction is a distinctive attribute of MAS fibers by which an unrestrained fiber can contract to about 40–50% of its initial length when immersed in water.<sup>13,14</sup> In previous investigations, it has been well established that the deformation of spider silk fibers produces large rearrangements of molecular chains, as explained below, although the details of this mechanism remain largely unclear. It is accepted that hydrogen bonding is the main interaction between molecular chains in the amorphous fraction, and the bonds are drastically reduced when the fibers are immersed in water. It has also been observed that nanocrystals reorientate and that the relative fractions of the three phases are modified by deformation. However, neither the details of the evolution of orientation and crystallinity, nor the overall relationship between microstructure and mechanical properties was depicted.

In the 1980s, pioneering studies by Work and Morosoff<sup>15</sup> showed that the crystalline unit cell dimensions remain unchanged when fibers supercontract, with the crystalline units being less oriented in supercontracted fibers. Grubb *et al.* studied the evolution of the microstructure during stretching by X-ray diffraction (XRD) in native<sup>7</sup> and supercontracted fibers.<sup>8</sup> In these works the authors identified the three phases in the material as isotropic amorphous, crystalline and oriented amorphous. In NMR studies the third phase is described as weakly oriented crystalline. In the above-mentioned work on supercontracted fibers the crystalline fraction was found to remain constant or even decrease when stretching the fibers, while it was proposed that the ordered amorphous fraction increases with deformation. In addition, the orientation of nanocrystals was found to grow with the deformation. Following a previous work by Riekel *et al.*,<sup>16</sup> Du *et al.* investigated by XRD the nanocrystal size as a function of the reeling speed, finding a greater fraction of highly oriented crystals for the higher speeds.<sup>17</sup> Glišović *et al.* measured by XRD the deformation and reorientation of nanocrystals in loaded fibers from different spiders, up to 10% of strain,<sup>18</sup> finding that the strain of the crystals is roughly 1/10 of the macroscopic strain. From the broadening of the Bragg peaks, they also estimated that the crystallite size perpendicular to the direction of the strain decreases with the applied load, which seems to be contradictory to the mentioned constancy of crystallinity. However, the broadening could also be explained by less-orderly growth of the crystallites of neighboring molecular chains. The strain in nanocrystals was also investigated by Brookes *et al.*, who correlated the shift in Raman spectra with the applied stress in spider silk fibers and the reeling speed,<sup>19</sup> and proposed a model of non-uniform stress in the material.

Apart from experimental studies, Termonia developed the widely accepted molecular model for spider silk,<sup>20,21</sup> which considers three components: nanocrystals oriented along the fiber axis, adjacent rigid chains and amorphous regions of elastomeric chains linked by hydrogen bonds. In the model, stretching of dry fibers produces the progressive rupture of the hydrogen bonds. The hydrogen bonds between chains are assumed to collapse when the fibers are immersed in water.<sup>13,14,22</sup> Finally, the detailed atomistic models developed by Ketten and Buehler predicted an increase in the fraction of the aligned  $\beta$ -sheets for high deformations,<sup>23</sup> which could produce an increase of the crystalline fractions. This increase has not been described

in the above-mentioned studies, though it is consistent with our results as explained below.

In this work, we have studied the microstructural changes of supercontracted MAS fibers during deformation. Previous studies have shown that the maximum supercontracted state represents a ground state for the material, to which it can revert independently from the previous loading history of the fiber. In particular, it is possible to obtain the whole range of tensile properties of the material by a process known as wet stretching<sup>24,25</sup> and the mechanical properties of the fibers can be unambiguously defined and controlled by means of the macroscopic alignment parameter  $\alpha$ .<sup>25</sup> This is a simpler option than the use of other more involved relationships that have subsequently been proposed to take into account the mechanical variability of MAS fibers.<sup>26–28</sup> Following this rationale, maximum supercontracted fibers have been subjected to different strains, *i.e.* different values of the alignment parameter  $\alpha$ , and analysed by X-ray diffraction and Raman spectroscopy.<sup>2,12,29</sup> The fibers have been stretched in hydrated condition, which allows obtaining fibers with high alignment<sup>25</sup> and which is the same condition considered in previous atomistic modeling studies.<sup>23</sup>

## II. Experimental section

### A. Obtaining silk fibers

We have used silk fibers from the major ampullate gland of *Argiope trifasciata* spiders. Given that it has been shown that MAS fibers from *A. trifasciata* share most of their specific features with those obtained from the other studied orbicularian spiders,<sup>30–33</sup> the main results reported below might also be extended to such species.

Spiders were bred in captivity and fed on a diet of crickets. Homogeneous MAS fibers were obtained by forced silking<sup>34</sup> at a speed of 10 mm s<sup>-1</sup> and nominal temperature of 20 °C and 35% relative humidity (RH). The silking force was measured during the process and about 1 m of continuous fibers obtained under constant force was selected. This condition ensures that the fibers are homogeneous.<sup>35</sup> The samples were obtained from that material and stored at 20 °C and 35% RH until testing. The initial state of the fibers after forcibly silking is labeled as FS, and usually corresponds to large values of the alignment parameter ( $\alpha \geq 0.9$ ).

### B. Supercontraction, wet stretching and mechanical tests: the macroscopic alignment parameter $\alpha$

By supercontraction, an unrestrained MAS fiber may contract to about 40–50% of its initial length when immersed in water.<sup>13,14</sup> As introduced above, the maximum supercontracted state (MS) can be used as a starting point from which the tensile properties of spider silk can be tailored in a reproducible way by stretching the fibers in water.<sup>25,36</sup>

The evolution of the tensile properties of the fibers with the alignment parameter has been analyzed by the authors in a previous paper,<sup>25</sup> where the experimental procedure for obtaining fibers with different alignment parameters is described. This procedure is sketched in Fig. 1. Initially, a fiber glued by its ends to an aluminium foil frame is immersed in water at 20 °C for 10 minutes. The fiber is allowed to contract, unrestrained, to the

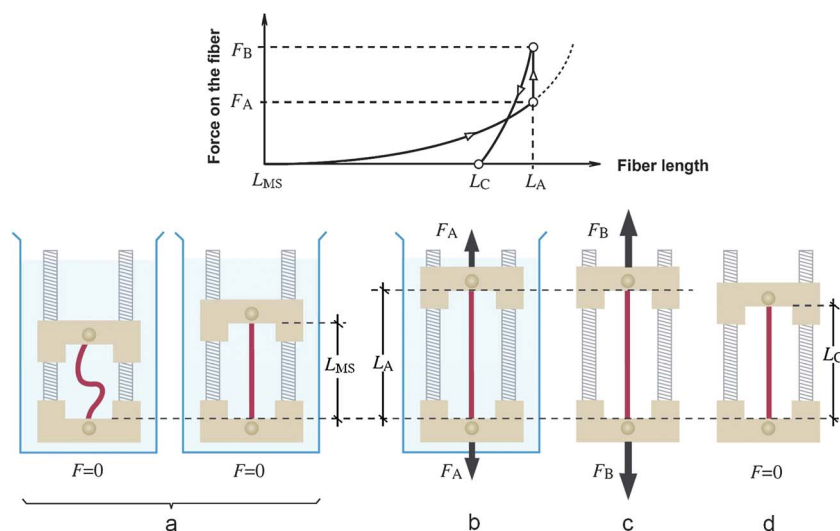


**Fig. 1** Procedure of obtaining fibers with different alignments  $\alpha$ : (a) initially the fiber is immersed in water and conditioned during 10 min; its initial length is  $L_{MS}$ ; (b) then the fiber is stretched up to the length  $L_A$ , and (c) dried overnight at fixed length; (d) the final length of the unloaded fiber after drying is  $L_C$ , and the alignment parameter is computed as  $\alpha = L_C/L_{MS} - 1$ . The room temperature was 20 °C.

maximum supercontracted length,  $L_{MS}$  (Fig. 1a). Then the fiber is stretched up to the selected length,  $L_A$ , and the ends are clamped in this position (Fig. 1b). Water is removed after 10 minutes and the fiber allowed to dry overnight at 20 °C and 35% RH (Fig. 1c). Stresses build up in the fiber during drying, probably due to the restoration of the hydrogen network that tends to shrink it.<sup>37,38</sup> Finally, the fiber is unloaded down to the final length  $L_C$  (Fig. 1d). The alignment state of a fiber is identified by the macroscopic alignment parameter  $\alpha$ , defined as  $\alpha = L_C/L_{MS} - 1$ . The alignment parameter of the forcibly silked (FS) samples is calculated as  $\alpha = L_{FS}/L_{MS} - 1$ ,  $L_{FS}$  being the initial length of the fiber after silking.

The mechanical properties of the fibers were measured as described elsewhere.<sup>37</sup> Silk fibers (base length = 20 mm) were mounted on aluminium foil frames and fixed in the grips of a testing machine (Instron 3309-622/8501, Canton, MA, USA) that was appended to an environmental chamber (Dycometal CCK-25/300, Barcelona, Spain). Forces were measured by a 100 mN load cell with 0.1 mN resolution (HBM 1-Q11, Darmstadt, Germany). Reproducibility was checked by testing one out of every five samples as a control. No significant deviation was observed in the tensile properties of the control samples.

To measure the diameters of the FS fibers, two small pieces (5 mm long) adjacent to both sides of each sample were retrieved, metallized with gold, and observed in a scanning electron microscope (SEM-JEOL 6300), at 10 kV and  $I = 0.06$  nA. The cross-sectional area was computed by assuming a circular cross-section and the mean diameter of a sample calculated as the average of at least five measurements. For MS and wet-stretched fibers, cross-sectional areas were derived from FS ones under the hypothesis of volume constancy<sup>39</sup> in all processes.

### C. X-Ray diffraction (XRD)

Synchrotron radiation microdiffraction experiments were performed at the ESRF-ID13 beamline by using an  $\sim 1 \times 1 \mu\text{m}^2$  monochromatic beam from crossed mirrors at a wavelength

$\lambda = 0.1$  nm, as explained in detail elsewhere.<sup>40,41</sup> A minimum of 90 observations were acquired on each sample, to obtain a mean diffraction pattern, and three to four samples were studied at each condition of alignment  $\alpha$ . Data analysis was performed with the FIT2D program.<sup>42</sup> Patterns recorded outside the fiber during a scan were used for background correction. XRD data were used to study the unit cell of the fibers, their crystallinity, the sizes of the nanocrystals and their orientation with respect to the macroscopic axis of the fiber.<sup>5</sup> We have used three different indexes to quantify the crystallinity of the fibers: (a) the ratio  $X$  between intensity arising from crystalline regions and total intensity for a fixed Bragg angle,<sup>8</sup> as described in the Results section; (b) the ratio  $\chi = \Sigma I_B/I_{\text{tot}}$  where  $\Sigma I_B$  is the sum of intensities of Bragg peaks and  $I_{\text{tot}}$  is the total intensity for the whole diffraction image;<sup>41</sup> and (c) the crystalline fraction  $X_C$  obtained by the method of Ruland following the scheme described by Grubb and Jelinski.<sup>7</sup>

The particle size was determined by Scherrer's equation,  $L = (0.9\lambda)/(B\cos\theta)$ , where  $B$  is the radial width (fwhm) of the Gaussian fitted for the diffraction spot.<sup>43</sup>  $L$  corresponds to a lower size limit for coherently scattering crystallites. Finally, the orientation of the nanocrystals was determined from the azimuthal broadening of the equatorial (210) reflections,<sup>44</sup> quantified by the full width at half maximum (fwhm) of the Gaussian functions used to fit the intensity profile.

### D. Raman spectroscopy

To measure the molecular alignment with respect to the fiber axis ( $z$  direction), polarized Raman spectra were collected with both the incident and scattered light either parallel ( $I_{zz}$ ) or perpendicular ( $I_{xx}$ ) to the fiber axis. A near infrared (NIR) diode laser (Toptica dfBeam 785-S with optical isolator) was used for excitation to reduce fluorescence emission from the sample. Laser light was focused on the fiber with a 100 $\times$  Mitutoyo Plan NIR infinity-corrected microscope objective. Laser power on the sample was kept below 20 mW. At this power the spectra did not

change with time, discarding any laser-induced damage. At least three different samples of each macroscopic alignment were analyzed. Scattered light was collected with the same objective and analyzed with a 300 mm focal-length single-grating spectrometer (Princeton Acton Spectra Pro 2300i) and a back-illuminated deep-depletion CCD detector (Princeton Pixis 256), thermoelectrically cooled ( $-75\text{ }^{\circ}\text{C}$ ) to reduce dark counts. Elastically scattered light was blocked with a long-wave pass edge filter (Semrock RazorEdge U grade). Polarization of the scattered light was selected by rotating a zero-order precision quartz  $\lambda/2$  wave plate before a fixed dichroic glass linear polarizer. A 1200 grooves per mm grating was used to measure the 1200–1700  $\text{cm}^{-1}$  range. This range was chosen because it contains the amide III and amide I bands. They arise, respectively, from vibrations approximately parallel and perpendicular to the polypeptide backbone and their intensity in polarized spectra is highly sensitive to the degree of orientation of the molecular chains.<sup>45</sup> For chains perfectly aligned along the fiber axis  $z$ , the amide I band is stronger in the  $I_{xx}$  spectrum, whereas the amide III band is stronger in the  $I_{zz}$  spectrum.

To compare quantitatively the degree of orientation, the empirical parameter  $p^2$  defined by  $p^2 = [I_{xx}(\text{I}) \times I_{zz}(\text{III})]/[I_{zz}(\text{I}) \times I_{xx}(\text{III})]$  has been used,<sup>2</sup> where I and III refer to the intensity of the amide I and amide III bands at 1668  $\text{cm}^{-1}$  and 1228  $\text{cm}^{-1}$ , respectively. For simplicity, the values used in the calculations were the intensities of the spectra at those wavenumbers. The parameter  $p^2$  cancels out any variations of intensity between  $I_{xx}$  and  $I_{zz}$  spectra due to focus or equipment sensitivity, and increases with the degree of orientation.

### III. Results and discussion

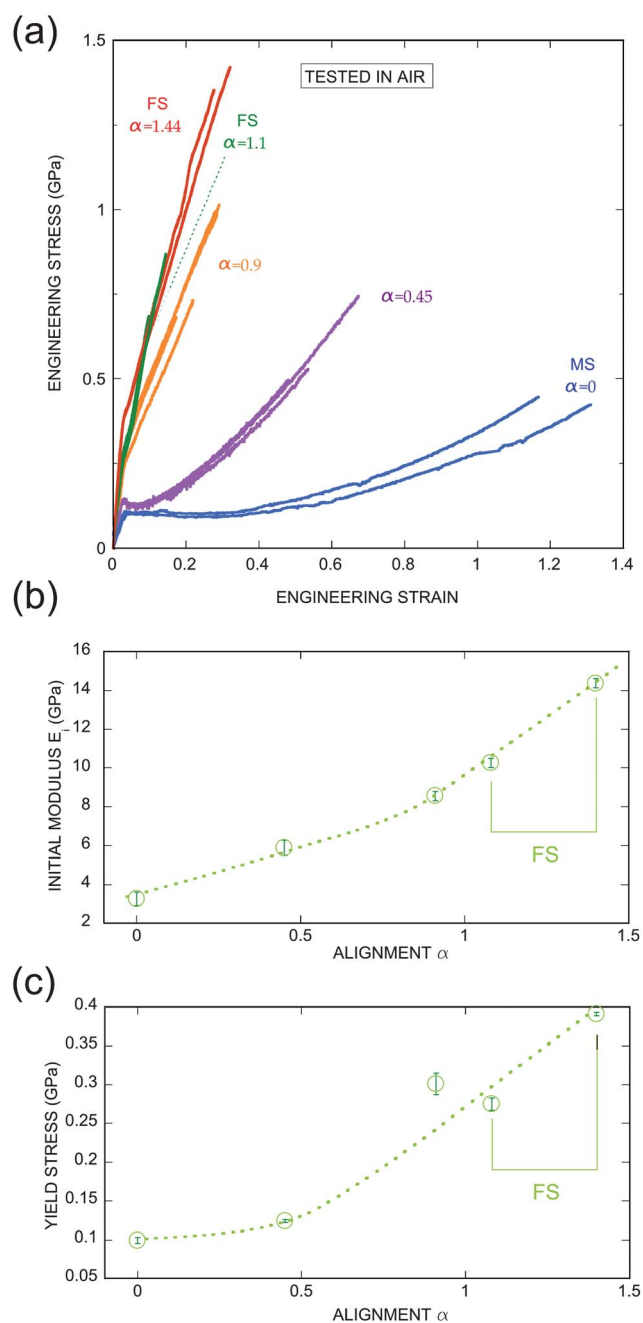
#### A. Mechanical behaviour

Fig. 2a shows the stress–strain curves for fibers with different values of the macroscopic alignment parameter  $\alpha$ . The curves show that the global stiffness and the stress at breaking increase with  $\alpha$ . The strain at breaking follows the opposite trend and, as expected for a polymeric material, the most aligned fibers show the lowest strain at breaking. The dispersion in the breaking strain and breaking stress values is high, as described previously and explained by a locally brittle behaviour.<sup>46</sup>

The initial elastic modulus, in Fig. 2b, and the yield stress (estimated as the proportional limit), in Fig. 2c, are represented as a function of the alignment parameter. Both variables increase with alignment and, interestingly, it seems that two regions could be identified: a slower growth for low values of  $\alpha$  and a higher increase of the elastic modulus and the yield stress above  $\alpha = 0.5$ . In particular, the yield stress is relatively constant for low values of the alignment parameter (0.10 GPa for  $\alpha = 0$  and 0.14 GPa for  $\alpha = 0.5$ ) increasing to about 0.3 GPa for  $\alpha = 0.9$ . These results will be discussed later in light of the microstructural study.

#### B. Crystallinity

Fig. 3 shows representative diffraction patterns for fibers with the four analyzed alignments ( $\alpha = 0, 0.45, 0.90, 1.44$ ). It can be seen that the azimuthal broadening of the Bragg peaks is lower for samples with higher values of  $\alpha$ , indicating a progressive orientation of the crystalline regions. The noticeable amount of noise



**Fig. 2** (a) Mechanical properties of fibers with different macroscopic alignments  $\alpha$ , tested under ambient conditions of 20  $^{\circ}\text{C}$  and 35% relative humidity. (b) Initial elastic modulus  $E_i$  vs. alignment  $\alpha$ . (c) Yield stress vs. alignment  $\alpha$ . The two higher values of alignment correspond to fibers as obtained by forced silking (FS). Error bars represent standard error.

present in the patterns can be explained by the small diameter of the fibers ( $\sim 3\text{ }\mu\text{m}$ ) in comparison with other thicker samples considered in other studies, such as MAS fibers from *Nephila clavipes* spider ( $\sim 5\text{ }\mu\text{m}$ )<sup>47</sup> or fibroin regenerated fibers ( $\sim 30\text{ }\mu\text{m}$ ).<sup>40</sup>

Previous X-ray studies identified the general crystal structure in silks as nearly orthorhombic containing anti-parallel  $\beta$ -pleated sheets.<sup>48</sup> The crystals are preferentially oriented with the molecular chains along the fiber axis and the brighter diffraction spots

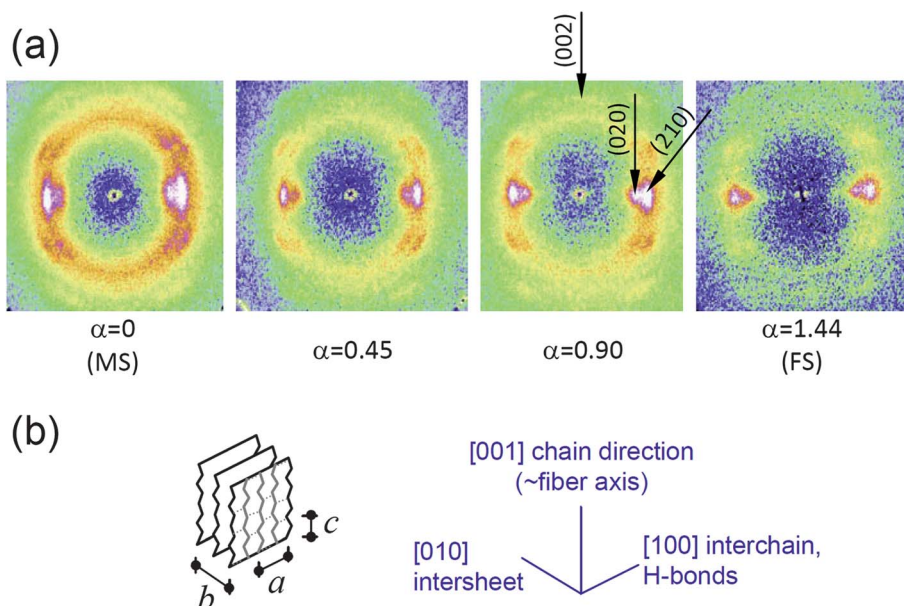


**Fig. 3** (a) Representative diffraction patterns of fibers for the four alignments studied. The three Bragg peaks considered to determine the characteristics of nanocrystals are indicated: (020), (210) and (002). (b) Sketch showing the crystalline directions and unit cell dimensions  $a \times b \times c$  in nanocrystals.

in the patterns correspond to the plane families (020) and (210). Their centers are in the so-called equator, which is perpendicular to the fiber axis. The centers of the reflections (002) are in the meridian direction which is parallel to the fiber axis. The azimuthal angle is defined so that it is equal to  $0^\circ/180^\circ$  for reflections (020) and is equal to  $+90^\circ/-90^\circ$  for reflections (002). We have calculated the unit cell dimensions from the reflections (020), (210) and (002) at each condition of alignment, see Fig. 3b, finding that the variation between different alignments is not significant, as previously described.<sup>15</sup> The calculated unit cell dimensions (mean value  $\pm$  standard error) are  $a = 0.997 \pm 0.001$  nm (interchain direction),  $b = 1.126 \pm 0.001$  nm (intersheet direction),  $c = 0.690 \pm 0.001$  nm (chain direction). These dimensions are similar to those found for other species and consistent with a high content of alanine, as discussed below.

The distribution of intensity in the pattern has been explained<sup>5,7,8</sup> as the superposition of: (i) the halo produced by the amorphous regions, (ii) the Bragg peaks produced by the  $\beta$ -sheet nanocrystals and (iii) part of the azimuthal broadening of the peaks produced by the weakly oriented regions. The existence of this last fraction of ordered material is supported by NMR studies<sup>6</sup> which suggested the existence of weakly oriented yet crystalline unaggregated  $\beta$ -sheets. This last fraction of ordered material has been also described as *oriented amorphous* material.<sup>7,8</sup> Fig. 4a illustrates the azimuthal distribution of intensity at the radial distance corresponding to the (210) peaks (scattering vector  $Q = 13.8 \text{ nm}^{-1}$ ) for an MS sample ( $\alpha = 0$ ). The intensity can be fitted as the sum of two pairs of Gaussian functions centered in each Bragg peak and a constant. The narrower Gaussians have been associated to the more perfectly crystalline material and the broader Gaussians to the less-perfectly ordered material,<sup>7,8</sup> the constant part being mainly due to the amorphous halo. This identification of Gaussian functions allows estimating the relative fraction of each component (which allows

comparison of different samples) although there is no reason why other distribution functions, different from Gaussian functions, could not exist, as already indicated.<sup>7</sup>

The areas representing the crystalline particles (C, areas under the narrower Gaussians), the weakly oriented material (O, areas under the broader Gaussians), and the amorphous material (A, area under the constant function) are displayed in Fig. 4b as fractions of the total area. It can be seen that for  $\alpha < 0.5$  the three fractions are approximately constant. However, for higher alignment the amorphous fraction decreases progressively, at the expense of the highly oriented nanocrystals and weakly oriented regions. Between  $\alpha = 0.5$  and  $\alpha = 0.9$  the most significant growth corresponds to the weakly oriented material and above  $\alpha = 0.90$  the reduction of amorphous material is compensated by the growth of the crystalline regions. The crystallinity index  $X$  is defined as the ratio between areas,  $X = (C + O)/(C + O + A)$ .

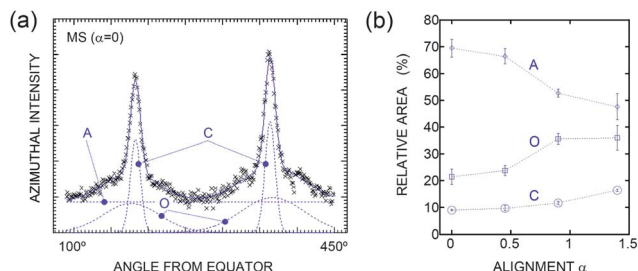


**Fig. 4** (a) Azimuthal intensity at the radial distance corresponding to the peak (210), i.e.  $Q = 13.8 \text{ nm}^{-1}$ , for an MS sample. The intensity is fitted by three different components: highly oriented nanocrystals (C, pair of two narrower Gaussians), weakly oriented material or 'oriented amorphous' material (O, pair of two broader Gaussians) and amorphous halo (A, constant function). (b) Relative area of the three components (area under the functions). Error bars represent standard error.

An alternative approach to quantify the crystallinity of the material is to analyze the intensity for the whole diffraction pattern. An important step is to separate the intensity arising from the crystalline reflections and the intensity of the amorphous halo.<sup>5,7</sup> For this purpose, the azimuthally integrated intensity can be analysed and fitted by intensity functions representing the different components.<sup>5</sup> Here, noise in the diffraction patterns made it extremely difficult to characterize the intensity of the Bragg peaks, and therefore it required an indirect characterization. The azimuthally averaged total intensity,  $I_T(Q)$ , has been computed as a function of the magnitude of the scattering vector  $Q = 4\pi\sin(\theta)/\lambda$ , or alternatively as a function of  $s = \sin(\theta)/\lambda$ . The azimuthally averaged intensity of the amorphous halo,  $I_A(Q)$ , has been calculated by azimuthal integration in selected regions where we considered that the intensity arising from Bragg peaks is negligible. These selected regions are indicated in Fig. 5a as shaded areas. The intensity of

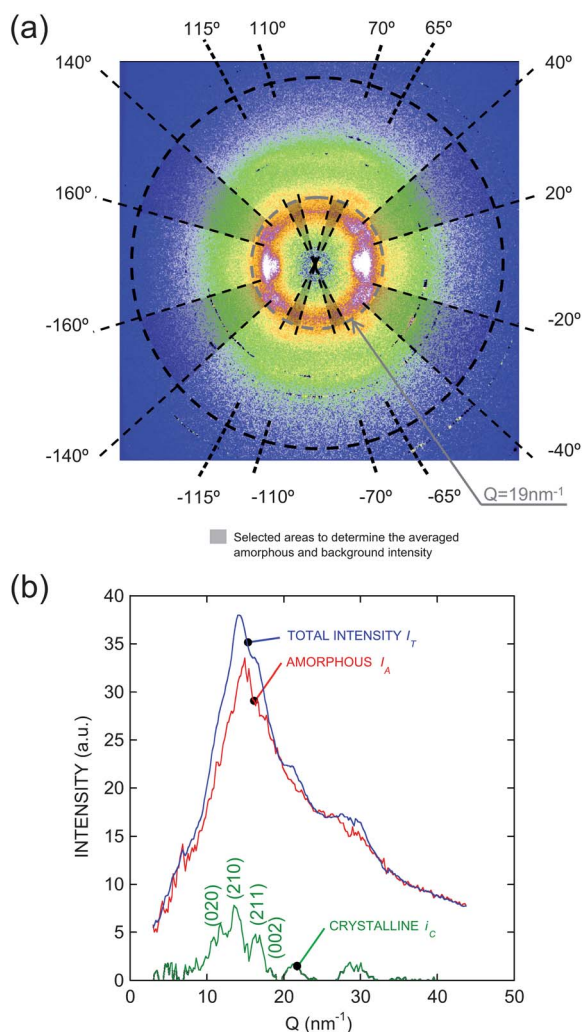


**Fig. 5** (a) Scheme of the areas selected to calculate, by azimuthal integration, the average intensity produced by the amorphous regions. In those areas the intensities of the Bragg peaks are considered negligible. The diffraction pattern of a MS fiber is shown as background. (b) Example of curves of azimuthally averaged intensities vs. the magnitude of the scattering vector  $Q$  for the same MS fiber.

Bragg peaks is then obtained as  $i_c(Q) = I_T(Q) - I_A(Q)$ . The intensity  $i_c(Q)$  includes the intensity produced by the highly oriented nanocrystals (associated above with the narrower Gaussian) and by the weakly oriented fraction which produces a higher broadening of the Bragg peaks (associated above with the broader Gaussian). As an example, the curves of intensity for one MS fiber are shown in Fig. 5b. It can be observed that the intensity  $i_c(Q)$  represents a small fraction of the total intensity.

The  $\chi$  index used to quantify the crystallinity is defined as the ratio between the integrated intensity of crystalline reflections and the integrated total intensity  $\chi = \int i_c(Q)dQ / \int I_T(Q)dQ$ .

A third crystallinity index, *i.e.* the crystalline fraction  $X_C$ , was obtained by the method of Ruland, from the curve  $R$  vs.  $s_p^2$ , as explained below in the Appendix. The curves calculated for the extreme conditions  $\alpha = 0$  (MS) and  $\alpha = 1.44$  (FS) are shown in Fig. 6 (the curves for  $\alpha = 0.45$  and  $\alpha = 0.90$  are omitted for clarity). Although the dispersion is considerable, it can be observed that the curves corresponding to each condition are spatially grouped. Each curve is approximated by a straight line (shown in the figure) and the intercept at  $s_p^2 = 0$  is taken as  $1/X_C$ .

The three indexes,  $X$ ,  $\chi$  and  $X_C$ , are displayed in Fig. 7 as a function of the macroscopic alignment parameter  $\alpha$ . Consistent with their definition, the trend in the evolution of the three is the same, indicating that the crystallinity is nearly constant between  $\alpha = 0$  and  $\alpha = 0.45$  and that it increases for higher values of  $\alpha$ . In the lowest alignment condition ( $\alpha = 0$ ), the estimated crystalline fraction is  $X_C = 17 \pm 4\%$  ( $\chi = 8 \pm 1\%$ ,  $X = 30 \pm 5\%$ ), while the fraction reaches the value  $X_C = 29 \pm 4\%$  ( $\chi = 15 \pm 1\%$ ,  $X = 52 \pm 10\%$ ) for the highest alignment ( $\alpha = 1.44$ ). The values of the indexes are given as mean value  $\pm$  standard error.

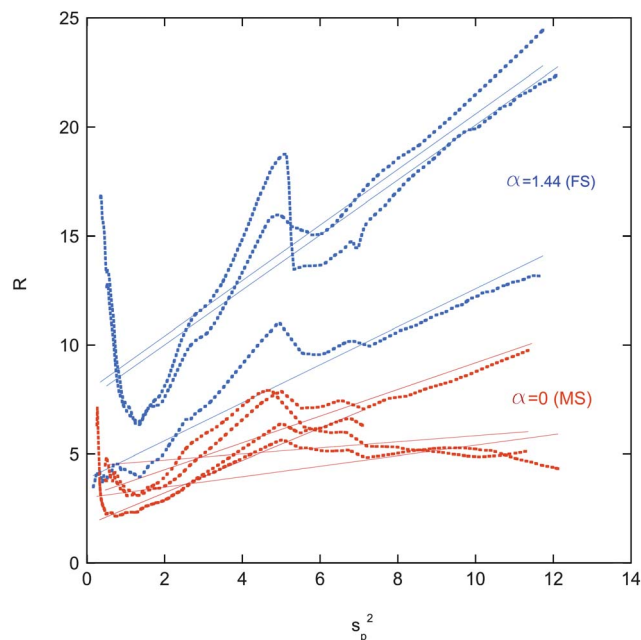


**Fig. 6** Ratio  $R$  vs. the upper integration limit  $s_p$  for MS and FS fibers (dotted lines). Each curve corresponds to one diffraction pattern. The linear regression of each curve is represented as a solid straight line. The intercept of each straight line with the vertical axis is  $R(0) = 1/X_C$ .

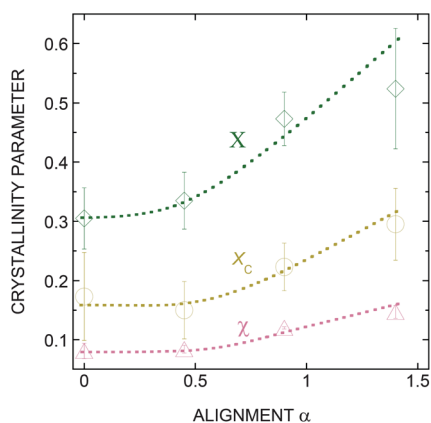


**Fig. 7** Crystallinity indexes calculated as the ratio between areas of intensity ( $X = (C + O)/(C + O + A)$ ), by the method of Ruland ( $X_c$ ) and by the ratio between the Bragg peaks' intensity and the total intensity ( $\chi$ ). Error bars represent standard error.

### C. Crystalline particle size

The sizes of crystalline particles were calculated from the radial profile of the 210, 020 and 002 reflections, and the results are shown in Fig. 8, which shows that there are no significant differences in the calculated size between the different conditions of alignment. The mean sizes in the three directions are respectively 3.6, 2.6 and 5.8 nm. From these values, the corresponding mean dimensions of the nanocrystals are  $5.2 \times 2.6 \times 5.8$  nm<sup>3</sup>, respectively along interchain, intersheet and chain directions (see the sketch in Fig. 3). These sizes range within the intervals determined in previous studies by XRD<sup>5,7</sup> and solid state NMR<sup>49</sup> for silks produced by other species, and indicate that the largest dimension corresponds to the direction parallel to the chains in the  $\beta$ -sheets (this dimension was obtained to be  $6 \pm 2$  nm by NMR).

### D. Orientation of molecular chains and crystalline particles

Full width at half maximum (fwhm), which quantifies the orientation of the crystalline regions, has been calculated from

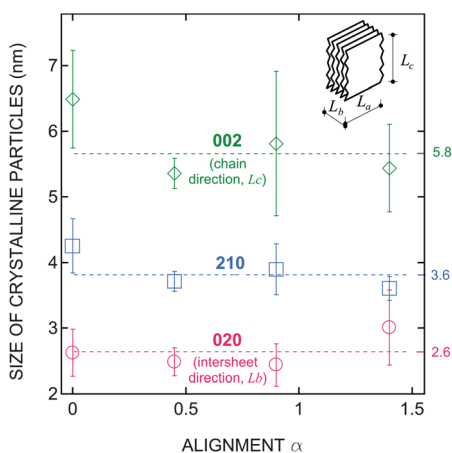


**Fig. 8** Size of the nanocrystals calculated by the Scherrer equation from the radial widths of the (020), (210) and (002) peaks. The three dimensions studied are shown in the sketch:  $L_a$ , in the interchain direction;  $L_b$ , in the intersheet direction; and  $L_c$ , in the chain direction. Error bars represent standard error.

the azimuthal fitting of the equatorial (210) reflections (see Fig. 4a), and it is represented in Fig. 9 as a function of the alignment parameter  $\alpha$ . It has been obtained for the narrow Gaussians, associated with the highly oriented nanocrystals, and also for the broader Gaussians, associated with the weakly oriented material. In the case of the highly oriented nanocrystals, the figure shows a step increase of the orientation (decrease in fwhm) between  $\alpha = 0$  and  $\alpha \approx 0.5$ , and an essentially constant value for  $\alpha > 0.5$ . In the case of the broader Gaussians, the results indicate that the latter ordered material remains weakly oriented, without significant variation of the orientation. Fig. 9 also shows the predicted fwhm for affine deformation. Under that hypothesis the tangent to the angle is proportional to  $(1 + \alpha)^{-3/2}$ .

It is expected that the mean orientation of the molecular chains along the fiber axis grows with the macroscopic alignment  $\alpha$ , which is confirmed by Raman spectroscopy. Fig. 10 shows polarized Raman spectra of the fibers at the different conditions of alignment. They contain the amide III band at approximately  $1228$  cm<sup>-1</sup> and the amide I band near  $1668$  cm<sup>-1</sup>. The amide III mode involves mainly the stretching vibration of the C–N peptide bond, oriented along the chain direction. The amide I mode consists mostly of the stretching vibration of the carboxyl C=O bond, oriented perpendicular to the chain direction. Thus, the analysis of the intensities of both modes allows characterizing the molecular orientation. This idea led us to utilize the parameter  $p^2$ , defined above, to quantify the protein chain alignment at the molecular level. The calculated values are collected in Table 1 as a function of the macroscopic alignment parameter  $\alpha$ . The parameter  $p^2$  ranges from 1.5 for MS ( $\alpha = 0.0$ ) samples to 4.0 for FS ( $\alpha = 1.44$ ) samples and increases almost monotonically with the macroscopic alignment. This tendency is not followed in the range of high alignments, since samples with alignment parameters of  $\alpha = 0.90$  and  $\alpha = 1.44$  show similar values of  $p^2$ , despite the amide III peak ( $1228$  cm<sup>-1</sup>) being more marked for the  $\alpha = 1.44$  sample, as Fig. 10 shows. The relative insensitivity of the

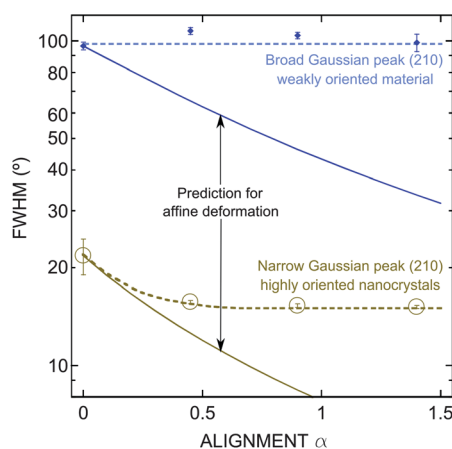


**Fig. 9** Full width at half maximum (fwhm) for the Gaussian functions obtained from the fitting of azimuthal intensity at (210) peaks (see Fig. 4). The narrow Gaussian is associated with highly oriented nanocrystals and the broader Gaussian is associated with the weakly oriented material. Smaller values of fwhm indicate a higher alignment of the crystals. Error bars represent standard error. The predicted fwhm for affine deformation is also included.

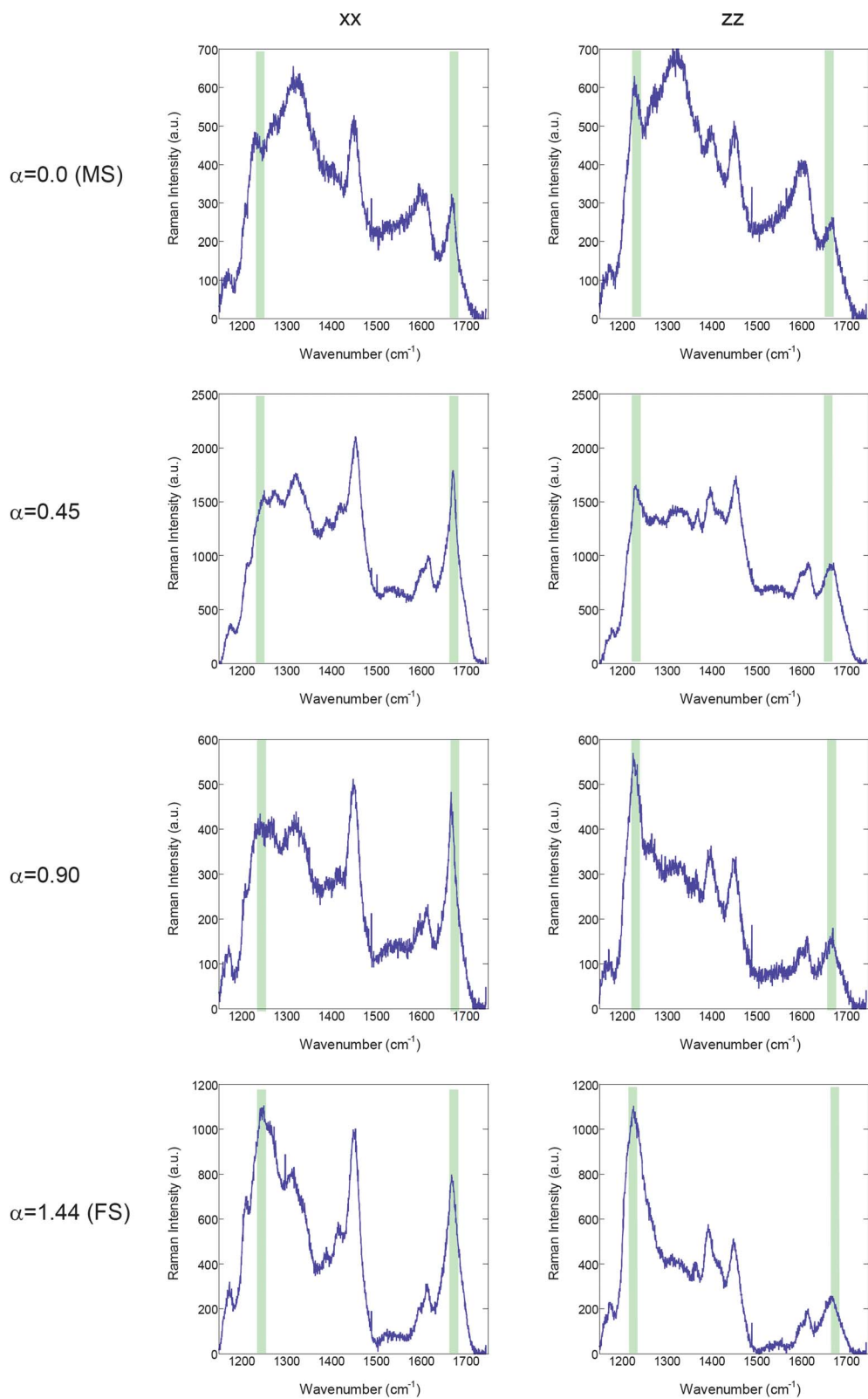


**Fig. 10** Representative Raman spectra for the four different alignments studied, collected with both the incident and scattered light either parallel ( $I_{ZZ}$ , right plots) or perpendicular ( $I_{XX}$ , left plots) to the fiber axis. The vertical lines indicate the wavenumbers of amide I (1668) and amide III (1228) bands.

**Table 1** Orientation parameter  $p^2$  (mean value  $\pm$  standard error) calculated from Raman spectra, for the four different alignments studied

Alignment $\alpha$	0.00	0.45	0.90	1.44
Orientation parameter $p^2$	$1.7 \pm 0.4$	$2.2 \pm 0.2$	$4.0 \pm 0.1$	$4.0 \pm 0.4$

$p^2$  parameter at high alignments can be related with the disappearing of an individual peak of the amide III vibration in the spectra taken at  $xx$  polarization, as observed in Fig. 10.

## E. Discussion

Warwicker studied the lattice dimensions for a large number of silks from different species,<sup>48</sup> finding that the dimension in the inter-sheet direction,  $b$ , was in the range 0.93–1.57 nm, while the other two dimensions remained constant:  $a = 0.944$  nm (inter-chain direction) and  $c = 0.695 \pm 0.005$  nm (chain direction). Later studies have shown a certain dispersion for these latter parameters,  $a = 0.930$ – $0.987$  and  $c = 0.690$ – $0.701$  nm.<sup>5,48,50–52</sup> In Warwicker's work the silks studied were grouped in five main groups, with distinct values for the dimension  $b$ . Our results for *Argiope trifasciata* MAS fibers yield a value  $b = 1.126$  nm, close to that for *Nephila clavipes* (Warwicker's group 3), and constitute an example of intermediate lattice, between Warwicker's group 3 ( $b = 1.06$  nm) and 4 ( $b = 1.50$  nm). The dimension  $b$  is twice the mean distance between consecutive  $\beta$ -sheets. Thus, it is higher in silks with larger side-chain residues in the crystalline regions. In the last years, the amino acid sequences (complete or partial) of some silks have been published, allowing analysis of the relationship between the content of short side-chain residues and the lattice parameter  $b$ . Warwicker considered alanine, glycine and serine as the short side-chain residues. The values of this dimension  $b$  and the percentages of short side-chain amino acids are listed in Table 2 for silks for which such data are well known. The correlation between both variables, since the greater values of dimension  $b$  correspond to the lowest percentages of short side-chains residues, is clear. This analysis is consistent with Warwicker's supposition that in silks with a lower content of short side-chain residues the relative contribution of large residues in the crystalline regions is higher.

The three methods utilized in this work to quantify the fraction of amorphous and ordered material yield qualitatively similar results: for  $\alpha = 0$  and  $\alpha = 0.45$  the fraction of amorphous material is reasonably constant and it decreases progressively for higher alignment. The estimated increase in the crystalline

fraction is likely linked to the increase in the general alignment of molecular chains, producing the incorporation of neighboring chains to the nanocrystalline particles. The three methods provide different values of the crystalline fraction. The first method allows an easy and simple comparison, although qualitative. The other two methods have been used previously to quantify the crystalline fraction.<sup>7,40</sup> The estimated crystallinity is between  $X_C = 17 \pm 4\%$  ( $\chi = 8 \pm 1\%$ ) for maximum supercontracted fibers with  $\alpha = 0$  and  $X_C = 29 \pm 4\%$  ( $\chi = 15 \pm 1\%$ ) for forcibly silked fibers with  $\alpha = 1.44$ . A practical outcome of this work is that the results confirm the validity of the three methods to compare qualitatively the microstructure of different samples in terms of fractions of ordered and amorphous material. Previous sequence studies<sup>3</sup> of *Argiope trifasciata* spider silks allow estimating the percentage of alanine to be  $\sim 23\%$  in number and  $\sim 20\%$  in mass. Poly(Ala) motifs are expected to be present in the nanocrystals, as discussed above, and in particular poly(GlyAla) motifs that flank the poly(Ala) motifs are present in the  $\beta$ -sheet structure.<sup>53</sup> Including glycine in GA motifs, the combined percentage of both amino acids is  $\sim 27\%$  in number. These percentages are close to the estimated crystallinity by the method of Ruland.

The crystallinity calculated covers the range of previous values obtained for MAS fibers from *Nephila clavipes* spiders:  $X_C = 12 \pm 3\%$  determined by X-ray diffraction<sup>7</sup> and  $\sim 35\%$  by NMR.<sup>6,53</sup> Moreover, solid state NMR studies of the structure<sup>53</sup> have shown that 34% of MA silk, obtained by forced silking from *Nephila clavipes*, is in  $\beta$ -sheet conformation. This would be the upper limit for the crystalline fraction, in agreement with our results. In such studies the alignment  $\alpha$  was not specified but, since the fibers are obtained by forced silking, a high alignment parameter can be assumed. For *Bombyx mori* silkworm silk fibers the reported crystallinity, estimated by XRD, is in the range 56–65%.<sup>41,54</sup> The higher crystallinity in *Bombyx mori* silk fibers agrees well with their higher stiffness and lower plasticizing effect of water compared to orb-web spider silk fibers.<sup>33,40,55</sup>

From the growth of the crystallinity with the macroscopic alignment  $\alpha$ , an increase of the size of nanocrystals could be expected. However, the estimated size is nearly constant within the experimental error. From  $\alpha = 0$  to  $\alpha = 1.44$ , the fraction of crystallites increases by a factor of  $V_{1.44}/V_0 \approx 29/17 \approx 1.7$ . If the increase in volume was produced by an isotropic growth of each nanocrystal, the variation of any length of a given nanocrystal would be  $L_{1.44}/L_0 \approx 1.7^{1/3} \approx 1.19$ . That difference of 19% is of the order of magnitude of the estimated error in the calculated particle sizes (Fig. 8). Besides, the calculated size depends both

**Table 2** Lattice dimension in the inter-sheet direction,  $b$ , and percentage of residues with short side-chains (alanine, glycine and serine) for silks spun by different species. The percentage has been computed from the sequences given in the references. The names of the sequenced proteins are indicated in parentheses. In *Bombyx mori*, the overall percentage of short side-chain residues is calculated for the unit heavy chain (HC) plus light chain (LC). In the four species of spiders, the percentage is obtained as the mean percentage of the two proteins present in the silk

Silk	Intersheet lattice parameter $b$ (nm)	Percentage of short side-chain residues (Ala + Gly + Ser)
<i>Bombyx mori</i> (fibroin LC + HC)	0.895–0.93 (ref. 48,50 and 57)	85.6% (ref. 58)
<i>Latrodectus hesperus</i> (MaSp1, MaSp2)	1.08 (ref. 52)	74.4% (ref. 59)
<i>Nephila clavipes</i> (MaSp1, MaSp2)	1.04–1.072 (ref. 5,7 and 51)	67.5% (ref. 60)
<i>Argiope trifasciata</i> (MaSp1, MaSp2)	1.126	65.3% (ref. 3)
<i>Araneus diadematus</i> (ADF-3, ADF4)	1.57 (ref. 48)	62.0% (ref. 61)

on the actual size of particles and the perfect-ordering degree in the crystal. Thus, the observed constancy of calculated sizes could be due to the growth of the diffracting particles accompanied by a less perfect order of the chains added to the nanocrystals.

The evolution of the orientation and the fraction of crystalline material indicate that there are two distinct regimes in the evolution of the crystalline regions (Fig. 11): (a) for macroscopic alignment below  $\alpha \approx 0.5$ , stretching the fibers produces the reorientation of the nanocrystals at constant crystalline fraction and (b) for further stretching an increase in the crystalline fraction is observed, while the nanocrystals remain highly oriented along the fiber axis.

The two regimes are also recognized in the mechanical behavior. The initial slope of the curve  $E_i(\alpha)$  is lower in the first

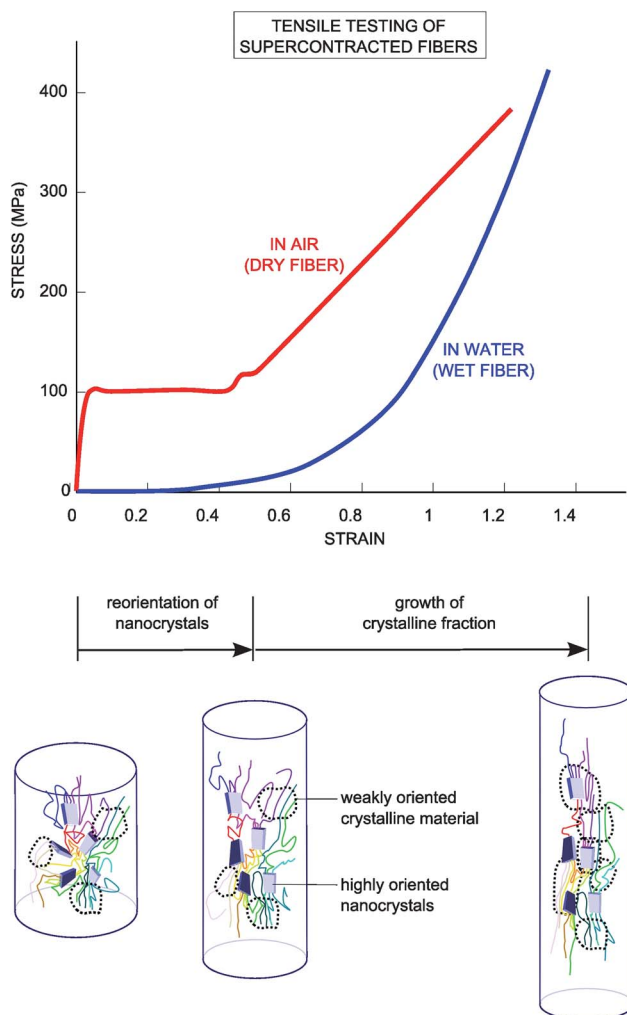


**Fig. 11** Sketch of the proposed two-regime model for the microstructural deformation of supercontracted spider silk fibers. During the first regime, the nanocrystals reorient until a maximum orientation of the chains along the fiber axis is attained for  $\alpha \approx 0.5$ . This first regime takes place at very low stresses if the fibers are stretched in water, and a plateau of constant stress is observed if the fibers are stretched in air. During the second regime,  $\alpha > \sim 0.5$ , the total fraction of crystalline material (both highly oriented nanocrystals and weakly oriented material) increases. Stretching the fibers in this latter regime requires a continuous increase of the applied stress.

regime than in the second regime (Fig. 2b). The reorientation of the nanocrystals and the chains in the amorphous material justifies the slow increment in the first regime, while the increase of crystalline fractions explains the faster increment of the modulus in the second regime. The linear variation of the elastic modulus  $E_i(\alpha)$  in the second regime can be easily explained by assuming a linear evolution of the crystalline fraction (Fig. 7) and using the law of mixtures: for a composite material with two phases undergoing equal deformations, the total elastic modulus  $E$  can be estimated as  $E = E_1 V_1 + E_2(1 - V_1)$ , where  $E_1$  and  $E_2$  are the elastic moduli and  $V_1$  and  $(1 - V_1)$  are the volume fractions of the two phases. Thus, this simple equation predicts that the total initial modulus  $E_i$  is proportional to the crystalline fraction, which grows practically linearly with  $\alpha$  (Fig. 7).

The identification of the two regimes is consistent with a previous atomistic model of the stretching of individual hydrated protein molecules.<sup>23</sup> In that work, the authors found that for strains lower than a certain value, corresponding approximately to  $\alpha \approx 0.5$ , the secondary structure proportion is constant, but for higher strains the percentage of chains in  $\beta$ -sheet conformation increases with the strain.

Regarding the yield stress, this can be identified as the stress required to break the hydrogen bonds which confine the nanocrystals and chains. Its value is practically constant for  $\alpha < 0.5$ , as expected since in this regime the fraction of the amorphous material remains essentially constant. For  $\alpha > 0.5$ , the yield stress increases progressively. In this second regime, the increasing of the crystalline fraction can be associated with an increasing in the stress required to break the hydrogen bonds between amorphous chains, due to the restrictions introduced by the new crystalline regions. Moreover, the increase of orientation of the molecular chains makes it possible to better balance the load over chains than at lower  $\alpha$ .

The procedure utilized in this work, *i.e.* the production of fibers with different alignments by stretching them in water, allows obtaining MAS fibers from *Argiope trifasciata* with high alignments.<sup>25</sup> The properties of the fibers, in particular the mechanical properties, have been shown to be essentially determined by the alignment  $\alpha$ ,<sup>25,56</sup> and thus we can assume that the microstructure would be reasonably similar if we had stretched the fibers in air. For maximum supercontracted fibers, the tensile curve (see Fig. 2b and 11) shows an initial linear region followed by the yield point and a long constant-stress plateau until a strain of about 0.5. Thus, in the plateau, after the yield point the reorientation of crystallites would take place without increment of stress. This reorientation would occur by rupture and new creation of hydrogen bonds, which are assumed to break easily above the yield point.<sup>20,21</sup> In the first regime, if the fibers are stretched in water, the orientation of the nanocrystals takes place at very low stresses, which is consistent with the plasticizing effect of water, which in turn produces the rupture of hydrogen bonds between chains.<sup>14,20,22</sup> In the second regime, further stretching of the supercontracted fibers requires a continuous increase of the applied stress, both in water and in air, which must be associated with the growth of crystalline fractions. In addition to the breaking and reorganization of the network of hydrogen bonds, the greater stress can be explained by the deformation of covalent bonds during the alignment of the molecular chains, required to form new crystalline/ordered material.

## IV. Conclusions

The study of MAS fibers with different alignments has allowed quantification of their content in amorphous material, highly oriented nanocrystals and weakly oriented material, and estimation of the orientation of both crystalline fractions. The crystalline fraction has been analyzed by three different methods, obtaining qualitatively congruent results. We have confirmed the validity of the very simple analysis of relative crystallinity based on the azimuthal intensity, when it is used to compare different samples.

The results are consistent with previous results from X-ray diffraction, NMR measurements and atomistic calculations,<sup>6–8,23</sup> providing additional details on the evolution of the microstructure. Two distinct regimes of the alignment of supercontracted fibers have been identified: for  $\alpha < 0.5$  the microstructural evolution is characterized by the reorientation of the nanocrystals, and for  $\alpha > 0.5$  the alignment modifies the relative fraction of crystalline material. The two regimes are also recognized in the evolution of the mechanical properties, which can be associated and explained by the microstructural changes.

These results provide important information on the relationship between microstructure and properties. The description of the two stages during the deformation of the fibers, separating the reorientation and the growth of the ordered material, will be highly valuable in developing and validating molecular models of the fibers.

The analysis of the lattice parameters in *Argiope trifasciata* and other silk fibers has provided new evidence of the relationship between amino acid sequences and lattice dimensions. The lattice dimension in the inter-sheet direction grows with the percentage of large side-chain residues as hypothesised by Warwicker in the 1960s.

## Appendix: the method of Ruland to estimate the crystallinity

The method of Ruland has been applied as follows. The intensity of Bragg peaks  $i_c(s)$  and the total intensity  $I_T(s)$  are obtained as a function of the scattering vector  $s = \sin(\theta)/\lambda$ , where  $\theta$  is the Bragg angle. These intensities are computed after polarization and geometrical correction using the program FIT2D. The structure-free coherent,  $I_{\text{coh}}(s)$ , and incoherent,  $I_{\text{inc}}(s)$ , scatterings were calculated from the chemical composition of the material, assuming a mean formula  $\text{H}_5\text{C}_3\text{NO}$ , and tabulated values of atomic form factors and incoherent scattering functions. The factor  $T$  was calculated as  $T = (I_{\text{coh}} + I_{\text{inc}})/I_T$  for the extrapolated values of intensities at  $s = 5 \text{ nm}^{-1}$ . This factor is used to remove the correct amount of incoherent scattering from the total intensity:  $i = I_T - I_{\text{inc}}/T$ . The ratio of corrected total intensity to intensity arising from crystalline reflections is then computed as

$$R(s_p) = \frac{\int_0^{s_p} i s^2 ds}{\int_0^{s_p} i_c s^2 ds}$$

Finally, a plot  $R$  vs.  $s_p^2$  is approximated by a straight line and the intercept at  $s_p = 0$  is taken as the inverse of the crystalline fraction,  $1/X_c$ .

## Acknowledgements

*A. trifasciata* spiders were provided and reared by O. Campos (ReptilMadrid, Madrid, Spain). This work was funded by the Ministerio de Ciencia e Innovación (Spain) (Grant MAT 2009-10258), by Comunidad de Madrid (Grant MADR.IB-CM/S-SAL/0312/2006) and by Fundación Marcelino Botín.

## References

- 1 F. G. Omenetto and D. L. Kaplan, *Science*, 2010, **329**, 528–531, DOI: 10.1126/science.1188936.
- 2 M. Elices, G. V. Guinea, G. R. Plaza, C. Karatzas, C. Riekkel, F. Agullo-Rueda, R. Daza and J. Perez-Rigueiro, *Macromolecules*, 2011, **44**, 1166–1176, DOI: 10.1021/ma102291m.
- 3 J. Gatesy, C. Hayashi, D. Motriuk, J. Woods and R. Lewis, *Science*, 2001, **291**, 2603–2605.
- 4 C. Y. Hayashi, N. H. Shipley and R. V. Lewis, *Int. J. Biol. Macromol.*, 1999, **24**, 271–275.
- 5 C. Riekkel, C. Branden, C. Craig, C. Ferrero, F. Heidelbach and M. Muller, *Int. J. Biol. Macromol.*, 1999, **24**, 179–186.
- 6 A. Simmons, C. Michal and L. Jelinski, *Science*, 1996, **271**, 84.
- 7 D. T. Grubb and L. W. Jelinski, *Macromolecules*, 1997, **30**, 2860–2867.
- 8 D. T. Grubb and G. D. Ji, *Int. J. Biol. Macromol.*, 1999, **24**, 203–210.
- 9 J. D. van Beek, S. Hess, F. Vollrath and B. H. Meier, *Proc. Natl. Acad. Sci. U. S. A.*, 2002, **99**, 10266–10271, DOI: 10.1073/pnas.152162299.
- 10 G. P. Holland, M. S. Creager, J. E. Jenkins, R. V. Lewis and J. L. Yarger, *J. Am. Chem. Soc.*, 2008, **130**, 9871–9877, DOI: 10.1021/ja8021208.
- 11 G. P. Holland, J. E. Jenkins, M. S. Creager, R. V. Lewis and J. L. Yarger, *Chem. Commun.*, 2008, 5568–5570, DOI: 10.1039/b812928b.
- 12 M. Rousseau, T. Lefevre and M. Pezolet, *Biomacromolecules*, 2009, **10**, 2945–2953, DOI: 10.1021/bm9007919.
- 13 R. W. Work, *Text. Res. J.*, 1977, **47**, 650–662.
- 14 G. R. Plaza, G. V. Guinea, J. Perez-Rigueiro and M. Elices, *J. Polym. Sci., Part B: Polym. Phys.*, 2006, **44**, 994–999, DOI: 10.1002/polb.20751.
- 15 R. W. Work and N. Morosoff, *Text. Res. J.*, 1982, **52**, 349–356.
- 16 C. Riekkel, M. Muller and F. Vollrath, *Macromolecules*, 1999, **32**, 4464–4466.
- 17 N. Du, X. Y. Liu, J. Narayanan, L. A. Li, M. L. M. Lim and D. Q. Li, *Biophys. J.*, 2006, **91**, 4528–4535, DOI: 10.1529/biophysj.106.089144.
- 18 A. Glišović, T. Vehoff, R. J. Davies and T. Salditt, *Macromolecules*, 2008, **41**, 390–398.
- 19 V. L. Brookes, R. J. Young and F. Vollrath, *J. Mater. Sci.*, 2008, **43**, 3728–3732, DOI: 10.1007/s10853-008-2597-y.
- 20 Y. Termonia, *Macromolecules*, 1994, **27**, 7378–7381.
- 21 Y. Termonia, in *Structural Biological Materials*, ed. M. Elices, Pergamon Press, Amsterdam, 2000, pp. 335–349.
- 22 J. M. Gosline, M. W. Denny and M. E. Demont, *Nature*, 1984, **309**, 551–552.
- 23 S. Keten and M. J. Buehler, *J. R. Soc. Interface*, 2010, **7**, 1709–1721, DOI: 10.1098/rsif.2010.0149.
- 24 J. Perez-Rigueiro, M. Elices and G. V. Guinea, *Polymer*, 2003, **44**, 3733–3736, DOI: 10.1016/S0032-3861(03)00245-3.
- 25 G. V. Guinea, M. Elices, J. Perez-Rigueiro and G. R. Plaza, *J. Exp. Biol.*, 2005, **208**, 25–30.
- 26 Y. Liu, Z. Z. Shao and F. Vollrath, *Nat. Mater.*, 2005, **4**, 901–905, DOI: 10.1038/nmat1534.
- 27 F. Vollrath and D. Porter, *Soft Matter*, 2006, **2**, 377–385, DOI: 10.1039/b600098n.
- 28 Y. Liu, A. Sponner, D. Porter and F. Vollrath, *Biomacromolecules*, 2008, **9**, 116–121, DOI: 10.1021/bm700877g.
- 29 A. Martel, M. Burghammer, R. J. Davies, E. Di Cola, C. Vendrely and C. Riekkel, *J. Am. Chem. Soc.*, 2008, **130**, 17070–17074, DOI: 10.1021/ja806654t.
- 30 R. W. Work, *Text. Res. J.*, 1976, **46**, 485.
- 31 J. Griffiths and V. Salanitri, *J. Mater. Sci.*, 1980, **15**, 491.
- 32 J. Perez-Rigueiro, M. Elices, J. Llorca and C. Viney, *J. Appl. Polym. Sci.*, 2001, **82**, 53–62.

- 33 M. Elices, G. R. Plaza, M. A. Arnedo, J. Pérez-Rigueiro, F. G. Torres and G. V. Guinea, *Biomacromolecules*, 2009, **10**, 1904–1910.
- 34 R. W. Work and P. D. Emerson, *J. Arachnol.*, 1982, **10**, 1–10.
- 35 M. Elices, G. V. Guinea, G. R. Plaza, J. I. Real and J. Perez-Rigueiro, *J. Mater. Res.*, 2006, **21**, 1931–1938, DOI: 10.1557/jmr.2006.0240.
- 36 M. Elices, J. Perez-Rigueiro, G. R. Plaza and G. V. Guinea, *JOM*, 2005, **57**, 60–66.
- 37 G. V. Guinea, M. Elices, J. Perez-Rigueiro and G. Plaza, *Polymer*, 2003, **44**, 5785–5788, DOI: 10.1016/S0032-3861(03)00625-6.
- 38 K. N. Savage, P. A. Guerette and J. M. Gosline, *Biomacromolecules*, 2004, **5**, 675–679, DOI: 10.1021/bm034270w.
- 39 G. V. Guinea, J. Perez-Rigueiro, G. R. Plaza and M. Elices, *Biomacromolecules*, 2006, **7**, 2173–2177, DOI: 10.1021/bm060138v.
- 40 G. R. Plaza, P. Corsini, E. Marsano, J. Perez-Rigueiro, L. Biancotto, M. Elices, C. Riekel, F. Agullo-Rueda, E. Gallardo, J. M. Calleja and G. V. Guinea, *Macromolecules*, 2009, **42**, 8977–8982, DOI: 10.1021/ma9017235.
- 41 A. Martel, M. Burghammer, R. J. Davies and C. Riekel, *Biomacromolecules*, 2007, **8**, 3548–3556, DOI: 10.1021/bm700935w.
- 42 A. Hammersley, FIT2D program, [www.esrf.fr/computing/scientific/FIT2D/](http://www.esrf.fr/computing/scientific/FIT2D/), 2009.
- 43 H. P. Klug and L. Alexander, *X-ray Diffraction Procedures for Polycrystalline and Amorphous Materials*, John Wiley & Sons, New York, USA, 2nd edn, 1974.
- 44 A. Misra, R. S. Stein, C. Chu, G. L. Wilkes and A. B. Desai, *J. Polym. Sci., Part C: Polym. Lett.*, 1975, **13**, 303–312.
- 45 M. E. Rousseau, T. Lefevre, L. Beaulieu, T. Asakura and M. Pezolet, *Biomacromolecules*, 2004, **5**, 2247–2257, DOI: 10.1021/bm049717v.
- 46 J. Perez-Riguerro, M. Elices, J. Llorca and C. Viney, *J. Appl. Polym. Sci.*, 2001, **82**, 2245–2251.
- 47 C. Riekel, C. L. Craig, M. Burghammer and M. Muller, *Naturwissenschaften*, 2001, **88**, 67–72.
- 48 J. O. Warwicker, *J. Mol. Biol.*, 1960, **2**, 350.
- 49 G. P. Holland, R. V. Lewis and J. L. Yarger, *J. Am. Chem. Soc.*, 2004, **126**, 5867–5872, DOI: 10.1021/ja031930w.
- 50 H. S. Sheu, K. W. Phyu, Y. C. Jean, Y. P. Chiang, I. M. Tso, H. C. Wu, J. C. Yang and S. L. Ferng, *Int. J. Biol. Macromol.*, 2004, **34**, 325–331, DOI: 10.1016/j.ijbiomac.2004.09.004.
- 51 A. Glisovic and T. Salditt, *Appl. Phys. A: Mater. Sci. Process.*, 2007, **87**, 63–69, DOI: 10.1007/s00339-006-3849-9.
- 52 J. E. Trancik, J. T. Czernuszka, F. I. Bell and C. Viney, *Polymer*, 2006, **47**, 5633–5642, DOI: 10.1016/j.polymer.2005.01.110.
- 53 J. E. Jenkins, M. S. Creager, R. V. Lewis, G. P. Holland and J. L. Yarger, *Biomacromolecules*, 2010, **11**, 192–200, DOI: 10.1021/bm9010672.
- 54 D. L. Kaplan, S. Lombardi, W. S. Muller and S. A. Fossey, *Biomaterials. Novel Materials from Biological Sources*, Stockton Press, New York, 1991.
- 55 J. Perez-Rigueiro, C. Viney, J. Llorca and M. Elices, *J. Appl. Polym. Sci.*, 1998, **70**, 2439–2447.
- 56 M. Elices, J. Perez-Rigueiro, G. Plaza and G. V. Guinea, *J. Appl. Polym. Sci.*, 2004, **92**, 3537–3541, DOI: 10.1002/app.20383.
- 57 R. E. Marsh, R. B. Corey and L. Pauling, *Biochim. Biophys. Acta*, 1955, **16**, 1–34.
- 58 Q. Y. Xia, Z. Y. Zhou, C. Lu, D. J. Cheng, F. Y. Dai, B. Li, P. Zhao, X. F. Zha, T. C. Cheng, C. L. Chai, G. Q. Pan, J. S. Xu, C. Liu, Y. Lin, J. F. Qian, Y. Hou, Z. L. Wu, G. R. Li, M. H. Pan, C. F. Li, Y. H. Shen, X. Q. Lan, L. W. Yuan, T. Li, H. F. Xu, G. W. Yang, Y. J. Wan, Y. Zhu, M. D. Yu, W. D. Shen, D. Y. Wu, Z. H. Xiang, J. Yu, J. Wang, R. Q. Li, J. P. Shi, H. Li, G. Y. Li, J. N. Su, X. L. Wang, G. Q. Li, Z. J. Zhang, Q. F. Wu, J. Li, Q. P. Zhang, N. Wei, J. Z. Xu, H. B. Sun, L. Dong, D. Y. Liu, S. L. Zhao, X. L. Zhao, Q. S. Meng, F. D. Lan, X. G. Huang, Y. Z. Li, L. Fang, C. F. Li, D. W. Li, Y. Q. Sun, Z. P. Zhang, Z. Yang, Y. Q. Huang, Y. Xi, Q. H. Qi, D. D. He, H. Y. Huang, X. W. Zhang, Z. Q. Wang, W. J. Li, Y. Z. Cao, Y. P. Yu, H. Yu, J. H. Li, J. H. Ye, H. Chen, Y. Zhou, B. Liu, J. Wang, J. Ye, H. Ji, S. T. Li, P. X. Ni, J. G. Zhang, Y. Zhang, H. K. Zheng, B. Y. Mao, W. Wang, C. Ye, S. G. Li, J. Wang, G. K. S. Wong and H. M. Yang, *Science*, 2004, **306**, 1937–1940, DOI: 10.1126/science.1102210.
- 59 N. A. Ayoub, J. E. Garb, R. M. Tinghitella, M. A. Collin and C. Y. Hayashi, *PLoS One*, 2007, **2**, e514.
- 60 M. Xu and R. V. Lewis, *Proc. Natl. Acad. Sci. U. S. A.*, 1990, **87**, 7120–7124.
- 61 P. A. Guerette, D. G. Ginzinger, B. H. F. Weber and J. M. Gosline, *Science*, 1996, **272**, 112–115.